A Differential Strand-Slot Inductance Model for Improved Compensation of Circulating Currents in the Core Part of Large AC Machines

Frederic Maurer, and Jonas Kristiansen Nøland, *Member, IEEE*

***Abstract*—The Roebel bar conventional design of large AC machines uses the classical strand-slot inductance model (CSSIM). Suitable alternatives are missing as the CSSIM is favored for its inherent simplicity based on the ideally permeable iron core hypothesis. However, saturated armature slots can lead to high variations of the slot inductance, where the CSSIM cannot represent this precisely. An accurate prediction of the strand inductances is crucial when optimizing the transpositions of large Roebel bars to be competitive on efficiency and low measurement tolerances. This fact is crucial in under-roebeling, having less than a 360-degree transposition over the active part. In the end, the goal is to compensate the winding overhang parasitic field with the slot-parasitic field. This paper proposes a differential strand-slot inductance model (DSSIM) based on the concept of differential inductance (DI). It is compatible with a circuital lumped-element model (LEM) that considers the strand topology, geometrical dimensions, saturation level, and small-scale effects. Numerical simulations showcase the performance improvement of the DSSIM against known models. Finally, a 20-strand prototype of a slot model with actual Robel bar strands corresponding to a simplified bar cross-section in a large AC machine's slot demonstrates the presented DSSIM's precision.**

***Index Terms*—Armature slots, circulating currents, differential inductance, Roebel bars, strand inductance.**

I. Introduction

CIRCULATING currents are causing useless additional joule losses in large electrical machines. They are, therefore, at scrutiny when optimizing the strand-slot design. A non-uniform loss distribution over the strands can cause bar damages, which has been documented since the 1970s for large AC machines. They can also cause uneven local forces [1] and eddy current dissipation [2]. In reference [3], circulating currents are measured using search coils. Moreover, in order to predict them more easily, novel analytical methods to compute the inductance have been proposed in [4], [5] without taking saturation and exact strand dimensions into account. A recent contribution [6] replies demonstrating that taking the strand geometry into account leads to better estimation of circulating currents, even though saturation is not influential in the end region. A general trend in other works [7]–[10] is analytically computing the circulating currents based on the lumped-element circuit model. In addition, the works of Liang et. al. and Haldemann [11]–[13] present compensation methods to reduce the circulating current. It is pointed out in [14]–[16] that the variation of the individual impedance of each strand determines the circulating currents, not only the strand inductance but also the effective AC strand resistance concerning the given strand configuration, which have also been studied in [17], [18].

F. Maurer and J. K. Nøland are with the Department of Electric Power Engineering, Norwegian University of Technology, Trondheim, Norway, 7034 NO (e-mail: frederic.maurer@ntnu.no).

Manuscript received May 28, 2021; Revised XY.

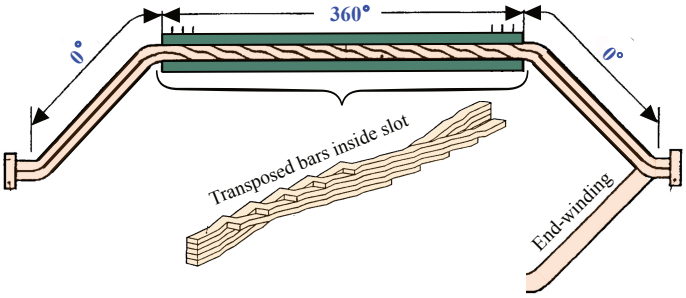

Fig. 1. Full length of roebel bar composed of strands short-circuited at both ends by brazing lugs through the stator slot of a large AC machine [16]. The cross-section of the iron core part is under investigation herein.

Non-uniform strand currents also imply local hot spots. In those hotspots, all the heat that dissipates locally will be transported through a three-dimensional thermal network [19]. A more accurate estimation of circulating current makes a global transposition method more effective [20]. Circulating currents can also get induced in the end-winding, where the bars usually are not transposed [6] (see Fig. 1). In this region, analytical formulations are very effective because of the magnetic linearity of air [21]. However, the unsaturated strand reactance in the core part is a factor 10 to 20 times bigger than in the end-winding [16]. This phenomenon occurs under armature short-circuit conditions according to the IEC60034 or applying the approach in [3]. In rated conditions, the strand-slot reactance ratio reduces by a factor 5 to 7 times when the armature slots are heavily saturated [16], having a significant impact on circulating currents, especially for large doubly-fed induction machines (DFIMs).

Under the consideration of under-roebeling, the variation between the different strand inductances in a slot becomes very important as it directly impacts the under roebeling effect. As shown in [15], a wrong computation of the optimal under-roebeling angle can negatively impact the circulating current by increasing them by a factor of 1.5 to 2 for even a tiny angular error. Therefore, one must rely on a highly precise strand-slot inductance model (SSIM) in the armature bars. This model has to take the actual strand geometry into

TABLE I
COMPARATIVE ASSESMENT BETWEEN CSSIM, DSSIM AND 3D-FEA.

Criteria	CSSIM	DSSIM	2D/3D-FEA
References	[4], [5], [7]	This work	[11], [22][3]
Saturation included	✗	✔	✔
Strand dimension accounted	✗[1]	✔	✔
Slot geometry considered	✗[2]	✔	✔
High precision	✗	✔	✔
Complexity	Low	Mid	High
Computational time	Low	Mid	Very high

[1] only height, no 2, or more in a column; [2] Simple; [3] Not full 3D-FEA.

account and the saturation level in the iron core. Earlier works, such as [4], [5], [7], [11], [22], proposed various approaches using both analytical and numerical approaches (i.e., magnetic field formulations, 2D-FEA and 3D-FEA) to compute strand-slot reactance to improve the analysis of circulating currents. The proposed DSSIM lies in between, taking advantage of heavy numerical analysis, but simplifies the implementation.

Table I presents a summary of the pros and cons of both the analytical and the numerical approaches. The main advantage of the analytical approach is its simplicity and low computational time, while its major drawback is its higher computational error ([16] and further highlighted in Fig. 10 of this paper). Numerical methods have basically the opposite pros and cons. A deeper analysis of the analytical models shows that they overlook the exact strand geometry and the saturation state of the electrical machine.

To showcase the benefits of the numerical approach in the context of low measurement tolerances, one performs FE analysis by investigating a single finite-length two-dimensional (2D) cross-section of the bar and its surrounding teeth and yoke. However, roebeling occurs in the three-dimensional (3D) axial direction, which can be taken into account using the concept of "permutation matrix" ([14]–[16]). Still, this 2D-trench is sufficient to guide the Roebel bar design by providing inputs to compute the strand inductance in the slot. The numerical pathway is usually based on finite element analysis (FEA) to study local sub-strand effects in detail [23]–[28]. However, the FEA needs a suitable analysis methodology to extract all the necessary information to guide the bar design.

This article proposes a differential slot-strand inductance model (DSSIM) based on the differential inductance (DI) concept to take the saturation and strand geometry into account [16]. It enhances the precision of the computation of the strand inductance in the slot, and therefore, reduces the computational error on the circulating current computation. However, it needs more computational time even though it is significantly less than a full time-stepping 2D- or 3D-FEA. Differential inductance (DI) is an FEA tool for more accurate circulating current estimation in the strands of the core parts of large AC machines based on the magneto-static FEA computations with the aim to achieve the same numerical precision as extremely time-consuming time-evolutive FEA computations. In particular, the DI effect is essential when considering the non-linear core's magnetization curve [29].

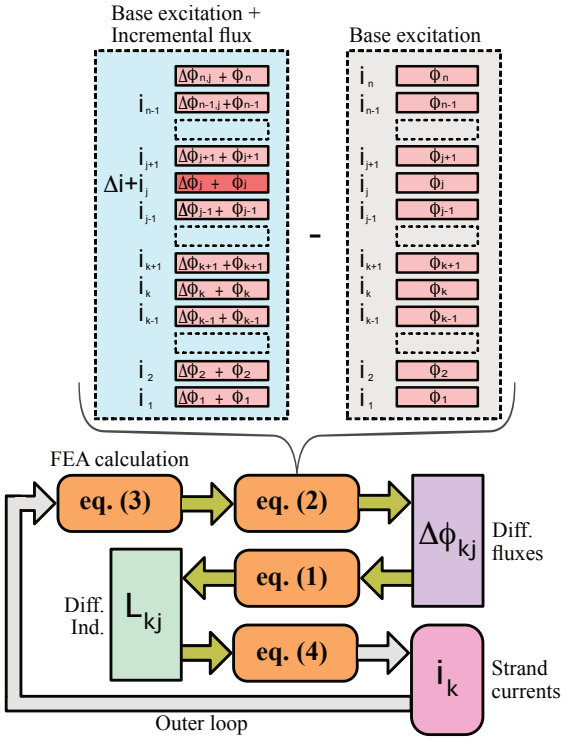

Fig. 2. Flowchart of DI approach. Green arrows are the mandatory inner loop. Grey arrows are the outer loop, which is optional. Eq. (2) is illustrated as an array of adjacent strands with and without the incremental flux.

The work was validated first using FEA and then with measurements on a small-scale armature slot specimen. It corresponds to the fundamental sub-strand cross-section part of a generic Roebel bar inside an armature slot, which refers to the mid-segment of Fig. 1. In addition to the numerical and experimental validation, this paper showcase a case study of a large AC machine, expanding on the implications of the presented method. The paper is organized as follows. Section II describes the DI model. Section III the experimental and numerical case studies, while section IV provides preliminary analysis exploring the DI's sensitivity. The main results, including the performance of the proposed DSSIM and its experimental validation, are provided in Section V before Section VI concludes the paper.

II. DIFFERENTIAL STRAND-SLOT INDUCTANCE MODEL

The concept of DI [30], [31] is the basis for the DSSIM. This concept postulates a local linearization of the saturation curve along a small current increment sweep. A complete description of the DI has already been made in [30], [31].

Consider an array of n individual strands enclosed in a bar of an armature slot (e.g., depicted in Fig. 2). At a given time instant (t), each strand carries individual currents, i_1, i_2, ..., i_n. If one of the strands has an incremental current added, Δi, the flux linkage of each strand will be slightly different (i.e., differential flux). In a nutshell, the DI (L_{kj}) of a strand

k with respect to another strand j, at a time instant (t), is

$$L_{kj} = \frac{\Delta\phi_{kj}}{\Delta i}, \tag{1}$$

where the differential flux linkage ($\Delta\phi_{kj}$) enclosed by strand k originated from strand j is obtained from

$$\Delta\phi_{kj} = \phi_k(i_1, .., i_j + \Delta i, .., i_n) - \phi_k(i_1, .., i_j, .., i_n). \tag{2}$$

The incremental flux linkage $\Delta\phi_{kj}$ is originated from a current increment added to conductor j (Δi). Individual flux linkages (ϕ_k) of strands k are calculated as the surface integral of the axial magnetic vector potential (A_z) as a post-processing of the field solution along the strand's cross-sectional surface, divided by its total surface area (S_k) and multiplied with its axial length (l_k), according to

$$\phi_k = \frac{l_k}{S_k} \iint_{S_k} A_z \mathrm{d}S. \tag{3}$$

The computation of a strand-slot DI matrix (L_{kj}) from eqs. (1)-(3) obeys the following procedure.

1) Know the strand currents (i_1,...,i_n) for each time step.
2) Calculate the static flux linkages of each strand (ϕ_k) from FEA post-processing using eq. (3).
3) Add a current increment (Δi) to branch current i_1 of strand number #1 (e.g., (typically 10 % of the actual current level in the strand)). Obtain the differential flux linkage $\Delta\phi_{k1}$ of each strand using eq. (2).
4) Compute the differential inductance components L_{k1}, from L_{11} to L_{n1}, using eq. (1).
5) Repeat steps 3) and 4) for all strands are until the entire inductance matrix L_{kj} is found for the given time step.

The procedure above is also depicted in Fig. 2.

The DI concept allows computing the strand inductance with a very high fidelity. However, it is also very time-consuming and computing-power intense. The above process is ideally repeated for each time step of an electrical period to be carried out. It leads to n_t x $(n+1)$ x n FE simulations (i.e., if no simplifications are made), where n_t is the total number of time steps, and n is the number of strands in the Roebel bar considered. For example, the computing resources needed for the large DFIM specified in Table III and depicted in Fig. 3 (a) could be considered.

As a thought experiment, one could assume that a single FE-simulation takes 1 minute to complete (considering a 2D-model, magneto-static simulation of 1 pole pair, i.e., $\approx$ 80 k elements using a single core computer). For the stator slot in our DFIM case, it leads to a simulation time of 128 x 129 x 1 mins = 11.5 days per time-step. This little example showcases the main drawback of this method, namely its huge computational effort, especially when not using high-performance computing (HPC) resources. Assuming the usage of an HPC with 128 cores, the computational time drops to 2.2 h per time-step, which is acceptable considering the significantly improved numerical precision. Still, it shows the need to simplify the implementation of the DSSIM.

To practically apply the DI concept, one needs to answer the following three general questions, which will be answered for the slot of a large AC machine:

1) Is the current increment, Δi, ideally emulating the maximal amplitude of the expected circulating current (e.g., 40 A for the experiment), leading to a linear approximation of the flux derivative ?
2) Are the DIs constant over time or not (i.e., is the DI variation below 0.1 % for the slot of the experiment)?

It is important to note that those questions must be answered for each application of DI separately, whereas the given numerical values can only be used for the specific case covered in this paper. There is no one-size-fits-all solution. Basically, if the first answer is "yes," then the method can be used without any restriction. A "no" would lead to such a huge increase in the computational effort - that it would not make sense to use DIs to solve the problem. The second question is only relevant for the computational costs as constant DIs over time lead to a significant reduction of calculation. The replies to the above-mentioned questions are provided in section IV.

III. Experimental and Numerical Case Study

This section briefly presents the case descriptions of the numerical and experimental investigations in this paper. Table II specifies the experimental setup which will be exploited in this paper, while Fig. 3 depicts its geometry. This setup has only 20 individual strand conductors to form a high enough Roebel bar to exhibit measurable circulating currents. It does not have any transpositions and lacks additional insulation between strands or between the bar and the slot, even though sufficient insulation for measurements is there. The strands are inserted in the slot carefully and held together at both ends by a clamping plate that acts as a current feeder, and a short-circuit as the brazing lug in classical Roebel bars. The prototype was also suitable to fit with the measuring capacities available at the laboratory. The current is measured using the non-invasive experimental approach to reach the highest possible accuracy. The addition of slight direct series resistances would significantly influence the realism of the results. This small-scale model is used as it has some advantages compared to large-scale models [6].

TABLE II
Strand-Slot Test Platform Specification

Symbol	Description	Data
	strand material	copper
	strand insulation material	daglas
	iron core material	M250-50A
b_{lam}	iron core lamination thickness	0.5 mm
	core insulation thickness	4-6 μm
n	number of strands	20
l_a	axial length	153.5 mm
w_s	strand width	7.4 mm
h_s	strand height	1.8 mm
r_s	strand edge radius	0.5 mm
b_i	insulation thickness	0.21 mm
R_s	strand resistance	$\approx$ 193.6 $\mu\Omega$

TABLE III
SIMULATED DFIM - MACHINE DATA

Symbol	Quantity	Value
S	apparent power	265.50 MVA
U_s	stator voltage	18 kV
I_s	stator current	8.5 kA
ω_m	mechanical speed	158.51 r/min
f_s	stator frequency	50 Hz
q_s	bars per slot (stator & rotor)	2
n_r	strands per rotor bar	38
n_s	strands per stator bar	64

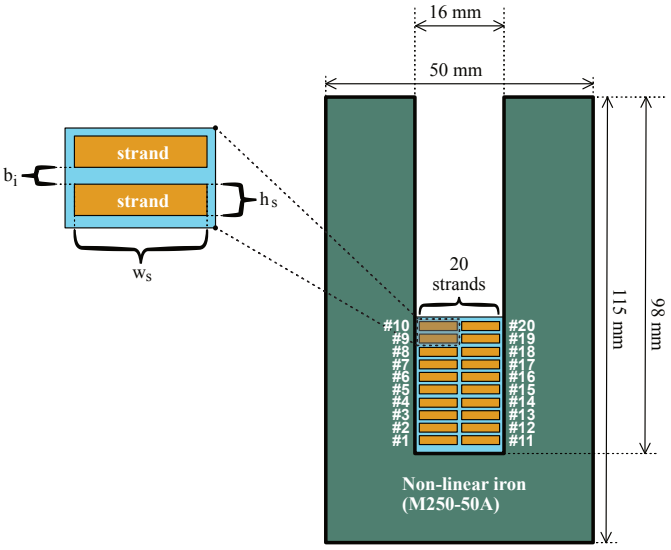

Fig. 3. Sub-strand section of the roebel bar slot experiment, including materials and dimensions related to Table II

The numerically studied large AC machine is a DFIM, specified in Table III. Moreover, its flux map is depicted in Fig. 4 (a). This type of machine is used in large-scale pump-storage hydropower plants, where the variable speed enables to vary the pump power to cope with intermittent renewable generation. A preview result flux map of of the experimental specimen is also depicted in Fig. 4, subfigure (b).

IV. DIFFERENTIAL INDUCTANCE SENSITIVITY STUDY

A preliminary sensitivity of the DI was conducted before implementing the proposed DSSIM. It was performed on a large DFIM using a 2D-FE model of the active part of the electrical machine and on the replica of the 20-strand experimental slot model. Fig. 5 shows the impact of varying the strand current on its own strand flux linkage at two handpicked time instants during the nominal load cycle of the DFIM. It can be seen that for a potential strand current variation within the normal range of a Roebel sub-strand experiencing circulating current, the strand flux is practically a linear function of its strand current. It is worth noting that the machine was operated at rated conditions with a sustained short-circuit between the strands at the bar edges, implying that the linear approximation of the differential inductance according to eq. (1) can be used for this problem regardless of the saturation level and time-step. It is perceived that this is because the strand current has only a minor impact on the saturation level of the AC machine. Thus, the hypothesis of linear simplification can be justified in this case study.

The strand current level can impact the results when applying the DI method on a smaller geometry, like in our experimental specimen. To highlight this postulate, we performed a magneto-static FEA for the geometry shown in Fig. 4 (b) using fixed currents. Strand #1 is located at the slot bottom and strand #10 at the top, both at the left column (see Fig. 3). In Fig. 6, the influence of the current increment level (Δi) on the DI highlighted. The DC current component of this increment was 0.5 A and 5 A, respectively. The self-inductance difference of the strands (i.e., #1, #5, and #10) between these increments were approximately $0.028\,\mu$H or about 1.8 %. However, the impact of this difference can be seen as negligible on the circulating currents because it is identical for all strands. It is also worth noting that the inductance grows unexpectedly with an increasing Δi. At the same time, one might expect the inductance to decrease with an increasing Δi, as a higher Δi means an increase of the saturation level, and therefore, a decrease of the inductance. Such observations make the DI distinct from the absolute inductance (AI). The simulation showed that the DI could be considered constant over time for any current level used in the laboratory. The maximal computed variation was 0.2367×10^{-4} nH or 0.023 % of the mean inductance [16].

To expand on the impact of this paper, a case study of the 265.50 MVA DFIM is included (see Table III for specifications or Fig. 3a for its flux map). In Fig. 7, the inductance matrix (L_{kj}) under nominal operation is presented. First, Fig. 7 (a) shows the time instant where the minimum L_{kj} values occur for the rotor strands. Here, the teeth are highly saturated, and the DI covers a range from $18\mu H$ to $21.5\mu H$. Further, Fig. 7 (b) depicts the same L_{kj} for another time instant at peak inductance values, where the teeth are non-saturated, exhibiting its typical DI matrix, covering a range from 22 μH to $35\mu H$. The values are approaching up to two times the saturated case. Both of these matrices are extracted from two-time instants under the nominal operating condition. These inductance variations must be considered in the context of large DFIMs, which are experiencing heavy teeth saturation during rated operation (1.9-2.1T induction can be considered as a normal value), which heavily impacts the slot strand inductance and then the circulating current computation [16]. It is also found by simulations that under sustained short-circuit operation, the DI is constant over time. In all other operating points, the DI is time-dependent and should be computed for each time step to achieve the highest amount of accuracy, if not simplifications are employed.

Fig. 7 (c) shows the time dependence of the self-inductance for several handpicked strands in both the rotor and the stator (i.e., top, middle, and bottom of the bar), which shows where the peaks and the minimal values occur during an electrical period. In general, the strand inductance is shown to vary significantly more for the rotor bars than the stator bars. In addition, the top bars closer to the air gap for both the

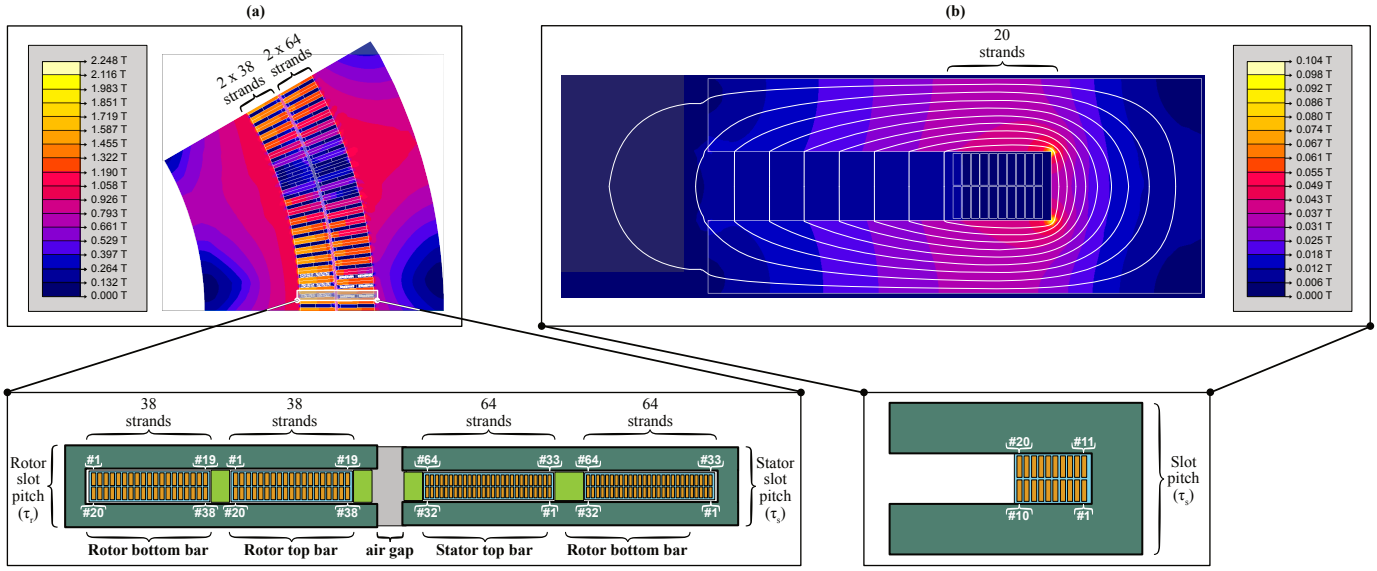

Fig. 4. Two-dimensional contour plot of the magnetic flux density from FE simulation conducted in Flux2D with injected currents for a particular time step. **(a)**: One pole-pair section of the DFIM at rated conditions (see Table III). **(b)**: 20-strand experimental slot model with a total slot DC current of 300 A.

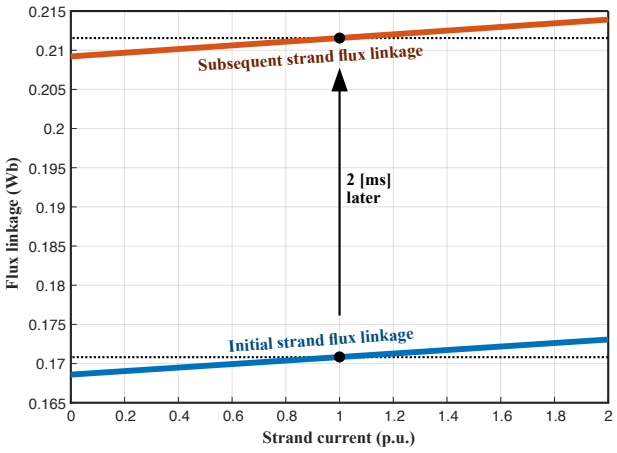

Fig. 5. Influence of the strand current (i_{38}) on the simulated strand flux for strand #38 of the top bar of rotor in Fig. 3 (a) at rated conditions (specified in Table III) for two separate time steps during the nominal load cycle. The base strand current were 39.5 A, i.e., 1501 A for the whole rotor bar.

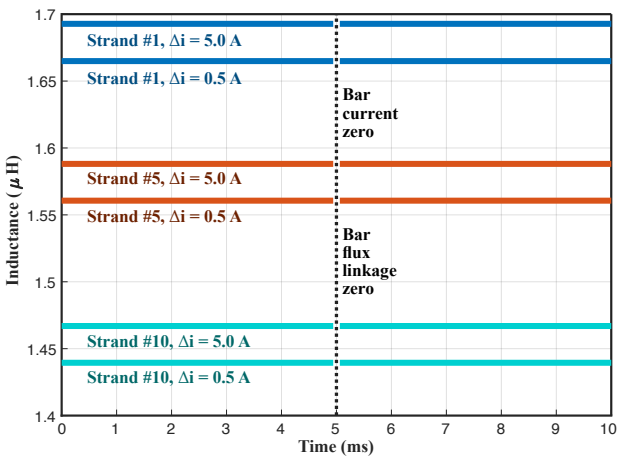

Fig. 6. Simulated influence of the strand current increment on the DI for different strands indicated in Fig. 3 (b) over time with $\Delta i = 0.5$ A. The AC-strand current is 5 A peak (50 Hz), with same phase for all strands.

rotor and the stator show much more variation in the strand inductance. In essence, the origin of this inductance time-variation is the variation of the main flux and the saturation of the teeth.

Finally, Fig. 8 highlights the impact of the operating point and the model employed (DSSIM vs. CSSIM). It shows the difference at nominal operation currents, between the time instant under highest saturation, the time step with the lowest saturation, as well the stator short-circuit case, using the DSSIM. The cases are then compared against the CSSIM with ideal load-independent iron as a base case [16]). All inductance values are presented in a scale normalized to the self-inductance inductance of the first strand located in the left column. In the saturated case, the inductance variation is the smallest, while in the short-circuit case, it is the highest. However, it is always less than in the ideal case using the CSSIM. On the contrary, for the stator short-circuit case, the inductance does not depend on the time. In this operation point, the stator and the rotor fluxes are in phase opposition and cancel themselves out. Finally, it leads to a minimal slot saturation so that the inductance remains constant over time. This highlights that the inductance variation and its precise calculation is a crucial factor to be taken into account, especially when studying under-roebeling and extended roebeling.

V. Assessment and Validation of the DSSIM

This section assesses the proposed DSSIM against the CSSIM, first numerically using simulation results and then comparing the obtained values against experimental results.

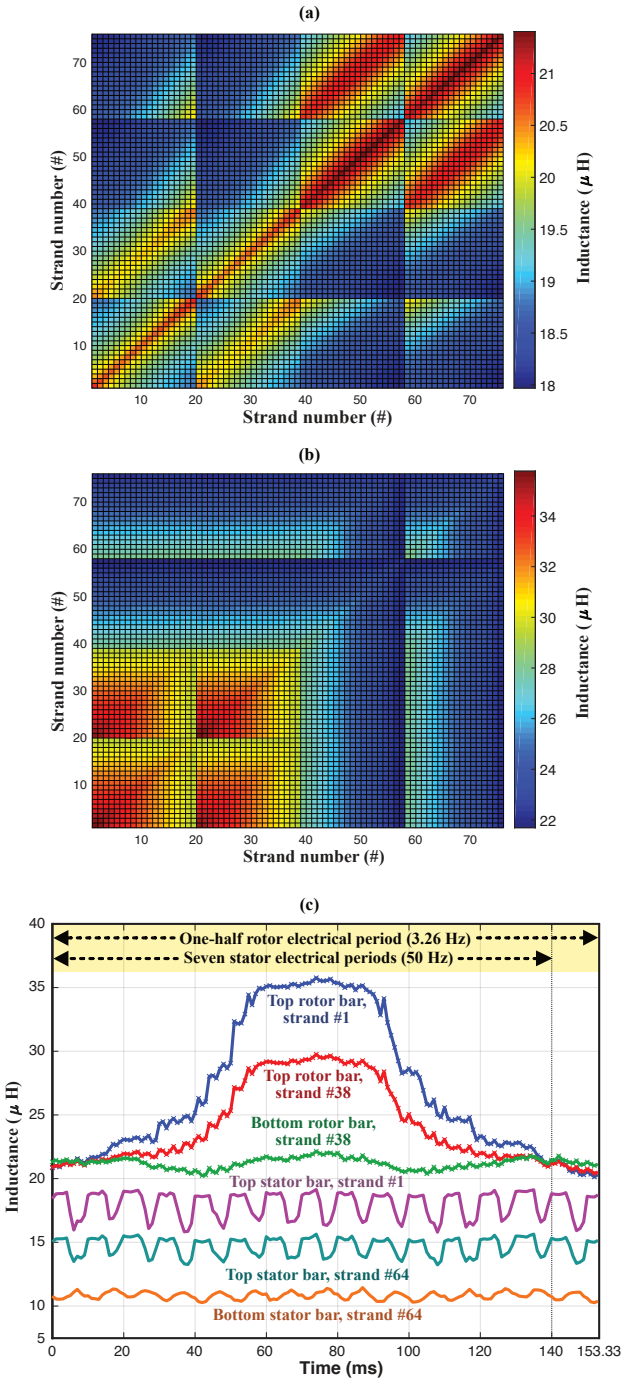

Fig. 7. Simulation study of the DI strand inductance time-influence at the nominal operation point over an electrical period for the 265.50 MVA DFIM machine (specified in Table III and flux map depicted in Fig. 3 (a)). #1 - #38 for bottom bar, #39 - #76 for the top bar. **(a)**: Saturated minimum value of strand inductance components (L_{kj}). **(b)**: Non-saturated peak value of strand inductance components (L_{kj}). **(c)**: Strand self-inductance over time.

A. *Establishment of the Circuital Model*

Fig. 9 presents the DI components (L_{kj}) of the experimental 20-strand slot model calculated using the proposed DSSIM, described in Section II. Fig. 9 (a) shows the self-inductance ($L_{1,1}$) and the mutual inductance ($L_{1,2}$ to $L_{1,20}$) of strand #1, whereas 9 (b) plots the complete 20 x 20 inductance matrix (L_{kj}) in a surface plot. Finally, Fig. 9 (c) assesses the deviation between the proposed DSSIM and the alternative CSSIM. The values obtained from the CSSIM were computed from analytical EQs. (4.3) and (4.5) provided in chapter 4 of a referred thesis dealing with this topic [16], based on [14], [15]. It can be seen in Fig. 9 (c) how the L_{kj} obtained from the CSSIM compared with the proposed DSSIM, had a deviation varying between 1.5 % and 1.9 %. The deviation provides insights into the origin of their discrepancies in the respective circulating current predictions of the DSSIM and the CSSIM, respectively. It is perceived that the conventional CSSIM behaves similar to the armature short circuit case, as there is no main flux, which magnetizes the iron core of the slot. As a result, it behaves like the stator short-circuit case presented in Fig. 8, which will be described in one of the following subsections.

The circuital lumped-element model (LEM) contains the slot, which is modeled primarily using the obtained DI matrix (L_{kj}), or an alternative matrix using the CSSIM. Moreover, there are also circuital effects outside the core part, including the end-winding strand inductance, the parasitic resistances using the actual copper length, and the skin effect additional resistance in the slot.

The circulating currents can be can be estimated as follows

$$\begin{bmatrix}1\\1\\...\\1\end{bmatrix} u_s(t) = \begin{bmatrix}R_1 & 0 & ... & 0\\0 & R_2 & ... & 0\\... & ... & ... & ...\\0 & 0 & ... & R_n\end{bmatrix} \begin{bmatrix}i_1(t)\\i_2(t)\\...\\i_n(t)\end{bmatrix} + \begin{bmatrix}L_{1,1} & L_{2,1} & ... & L_{1,n}\\L_{2,1} & L_{2,2} & ... & L_{2,n}\\... & ... & ... & ...\\L_{n,1} & L_{n,2} & ... & L_{n,n}\end{bmatrix} \begin{bmatrix}\frac{di_1}{dt}\\\frac{di_2}{dt}\\...\\\frac{di_n}{dt}\end{bmatrix}, \quad (4)$$

where $u_s(t)$ is the applied source voltage over the slot, and the feeding resistance is neglected. This is the circuital LEM approach used for both the DSSIM and the CSSIM.

B. *DSSIM vs. CSSIM*

A numerical comparison has been performed using a time-stepping 2D-FE simulation of the same slot model emulating the experimental setup (i.e., also used to extract the circuital inductance), incorporating the measured absolute BH-curve of the iron sheets (i.e., M250-50A). The assessment was done by comparing the LEM-computed circulating currents using the CSSIM against the proposed DSSIM, with a time-stepping FE simulation considered as the base case. The circulating currents in the circuit approach were found using a LEM equivalent obtained from eq. (4), with resistive elements corresponding to the strands computed using the DC-resistance formula (for the numerical value, refer to Table II) [16]. The skin effect coefficient lies between 0.0159 % and 4.4907 %

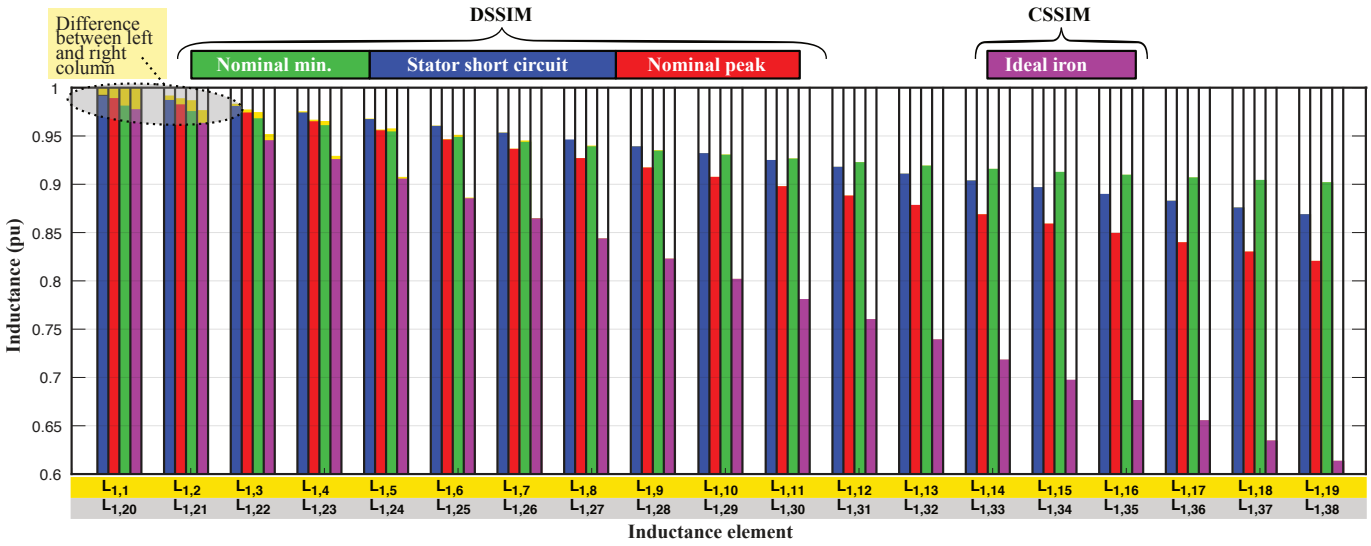

Fig. 8. Rotor top bar strand DI for the 265.50 MVA DFIM machine (specified in Table III and flux map depicted in Fig. 3 (a)) under different conditions, i.e., minimum and maximum point during nominal operation, stator short-circuit point, and ideal iron core case. Yellow areas on top of the bars indicate the DI difference between $L_{1,1}$ and $L_{1,20}$, $L_{1,2}$ and $L_{1,21}$, and so on.

with a mean value of 1.6553 % (more details given in [16]). This is found from the classical approach used to compute skin effect for strands in an ideal slot, which have been added to the DC-resistance of each strand, i.e., R_1 to R_{20}, respectively. The skin effect was found to have the biggest impact on the resistance on the highest located strands (i.e., R_{10} and R_{20}).

The deviation in strand inductance components given in Fig. 6 manifests in the predicted circulating currents. Fig. 10 clearly shows that the DSSIM performs significantly better than the CSSIM for all strands (both columns, due to symmetry, give the same results up to 3 significant digits). The error for the DSSIM is below 1.2 % against the time-evolutive FE model, traducing an excellent numerical precision of this model and a significant precision enhancement of this approach compared to the CSSIM. In comparison, the CSSIM always has a higher error than the DSSIM with a peak value at 8.5% on currents, meaning over 17% on losses. In the context of high competition towards efficiency increase and reduction of measurement tolerances on efficiencies in hydro-generators[1], there is a strong need for more precise computation methods and the DSSIM clearly responds to this need.

In order to expand on the error improvement of the DSSIM compared to actually known models, a comparison with another analytical approach have been added on Fig. 10, namely the "multiple mirror-method" (or ASSIM - Absolute-Slot-Strand-Inductance-Method)[2] (refer to [16]). This method takes the strand geometry and position perfectly into account but considers the iron as infinite permeable. Thus only, the saturation component is missing with respect to the DSSIM. As it can be seen, the DSSIM has here also a significantly lower difference compared to transient FEA for strands 1-4. For the higher strand number, the error is in the same range as for the DSSIM. This allows us to conclude that the geometry is the preponderant factor for the higher located strands, while taking the non-linear iron into account is the dominant factor for the lower strands in the case of a short-circuited slot. Again, the DSSIM offers the best precision over all strands in all simulated cases.

[1]In today's tender, the IEC tolerance does not apply anymore. The clients are only accepting a reduced tolerance of about 2-3%.

[2]One could also obtain the same results as performing FEA analysis on a slot with infinite permeable iron.

C. Experimental Validation of the DSSIM

Fig. 11 presents the photo and the schematic view of the experimental setup used to validate the proposed DSSIM. The actual slot was 153.5 mm deep and is composed of stacked, insulated (with 4-6μm of lack) and pressed electrical steel sheets, which have been laser cut like in the stator of large electrical machines. The hybrid clamping system is yellow-white and tightened using red bolts and squared nuts. At both ends of the strands, there are two copper connection devices to ensure the proper experiment current feeding of around 350 A (RMS) at maximum. On the left side of Fig. 11 (a), the conductors were widened to decrease the magnetic coupling at the hall sensors. One can also see the glued hall sensors and the strand fastening system, which function is used to tighten the strands together to enable precise calibration of the measurements.

The slot is only saturated by the current flowing through the conductors; It was not possible to add another conductor or coil to simulate the main flux saturation of the slot due to power source constraints in the laboratory.

The current measurement is indirect and uses hall-sensors to convert the strand current-induced magnetic field into a voltage collected using a precision time-recording device. As the distances are short, the flux density generated by the different strands can be measured by the hall-sensors associated with adjacent strands. The complete relationships

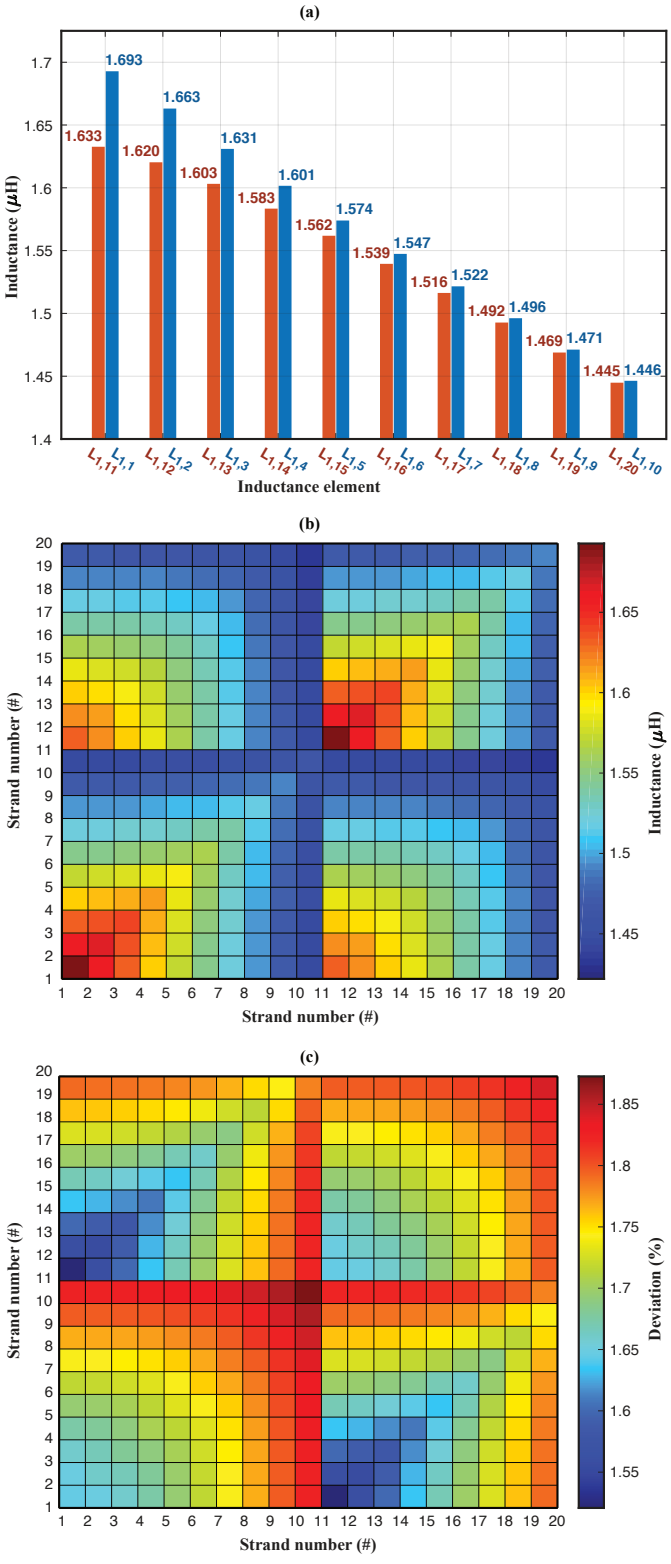

Fig. 9. Differential inductance matrix (L_{kj}) calculated for the 20-strand slot experimental model (see Figs. 2 and 3 (b)) with an instantaneous current in each strand of 5 A. **(a)**: Self- and mutual inductance of strand 1. **(b)**: Complete inductance matrix. **(c)**: Deviation of the conventional CSSIM against the proposed DSSIM with DSSIM as the base.

of these phenomena can be formulated relating voltages to

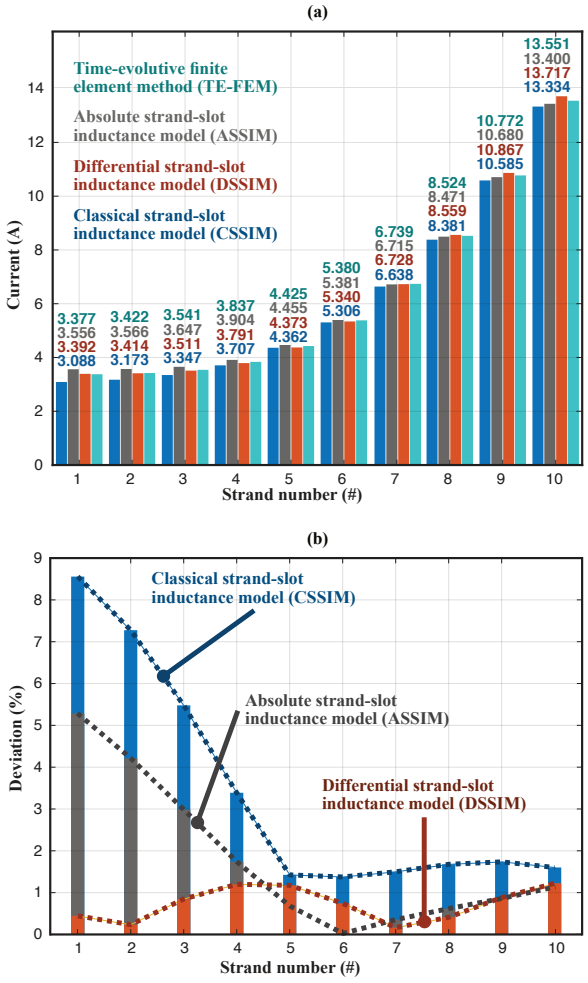

Fig. 10. Investigation of circulating current in the 20-strand slot model depicted in Fig. 3 and Fig. 4 (b), comparing conventional CSSIM and ASSIM models against the proposed DSSIM, with the time-evolutive finite element method (TE-FEM) as a reference. The AC current loading penetrating the slot were 100 A (rms). **(a)**: Absolute values (rms). **(b)**: Deviations.

currents using the following calibration matrix ($\mathbf{A_{mat}}$)

$$\begin{bmatrix} u_1(t) \\ u_2(t) \\ \dots \\ u_n(t) \end{bmatrix} = \underbrace{\begin{bmatrix} a_{1,1} & a_{2,1} & \dots & a_{1,n} \\ a_{2,1} & a_{2,2} & \dots & a_{2,n} \\ \dots & \dots & \dots & \dots \\ a_{n,1} & a_{n,2} & \dots & a_{n,n} \end{bmatrix}}_{\mathbf{A_{mat}}} \begin{bmatrix} i_1(t) \\ i_2(t) \\ \dots \\ i_n(t) \end{bmatrix}, \quad (5)$$

where measured voltages (u_1, u_2,..., u_n) are related to individual strand currents (i_1, i_2,..., i_n). As an example, the first column of the calibration matrix, $a_{1,1}$ to $a_{n,1}$, can be found injecting a known current through the first strand (i_1), while keeping the other strands open-circuit. Each coefficient in the first column of the calibration matrix is then calculated as

$$a_{k,1} = \frac{|u_k|}{|i_1|}, \quad (6)$$

where $|u_k|$ is the amplitude of the measured hall-sensor voltage (k refers to the strand number) and $|i_1|$ is the amplitude of the current fed through strand #1. Both amplitudes were determined using curve fitting. The same procedure is repeated for all columns in the calibration matrix. Finally, the

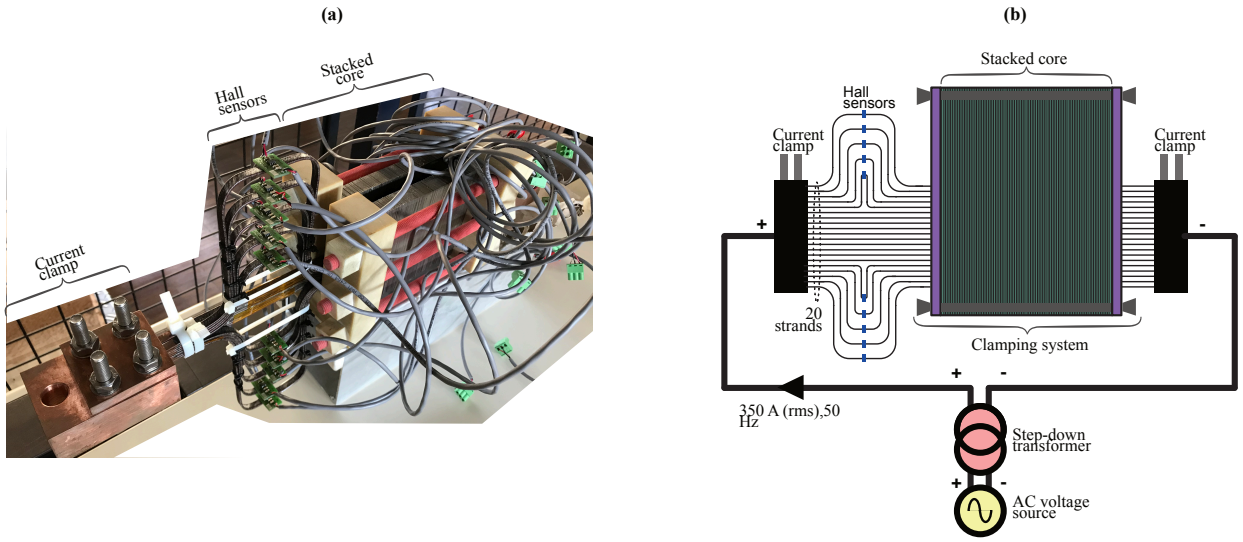

Fig. 11. Strand-slot test platform specified in Table I and Fig. 2. **(a)**: Photo of the setup. **(b)**: Schematic circuit drawing.

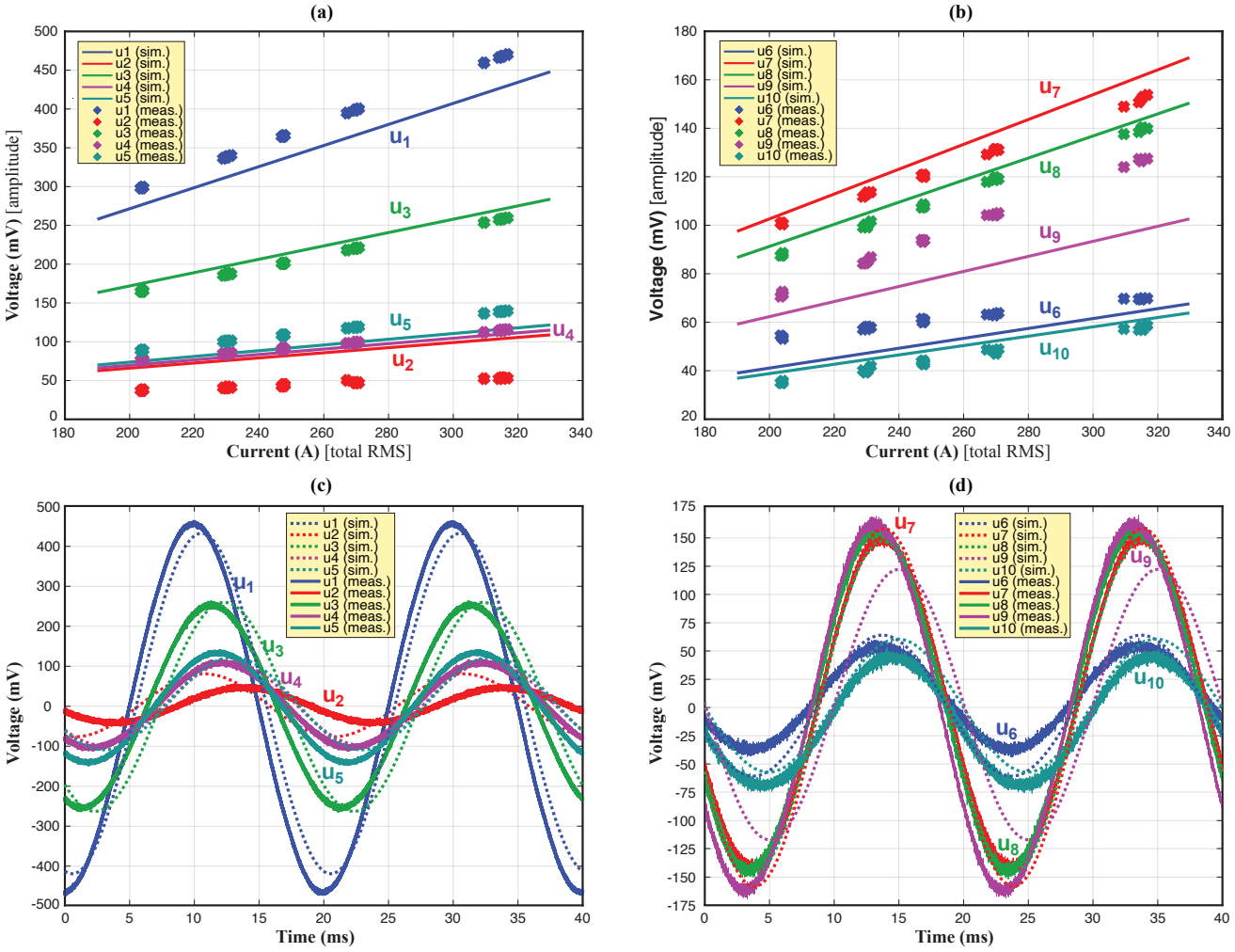

Fig. 12. Validation of the slot experiment against the simulation model. **(a)**: Branch voltages u_1-u_5 (amplitude) as a function of total slot current current (rms). **(b)**: Branch voltages u_6-u_{10} (amplitude) as a function of total slot current current (rms). **(c)**: Time series of branch voltages u_1-u_5 with the total slot current equal to 309.52 A. **(d)**: Time series of branch voltages u_6-u_{10} with the total slot current equal to 309.52 A.

measured voltages can be used to predict the instantaneous strand currents by inverting the calibration matrix as follows

$$\begin{bmatrix} i_1(t) \\ i_2(t) \\ \dots \\ i_n(t) \end{bmatrix} = \underbrace{\begin{bmatrix} a_{1,1} & a_{2,1} & \dots & a_{1,n} \\ a_{2,1} & a_{2,2} & \dots & a_{2,n} \\ \dots & \dots & \dots & \dots \\ a_{n,1} & a_{n,2} & \dots & a_{n,n} \end{bmatrix}^{-1}}_{\mathbf{A_{mat}^{-1}}} \begin{bmatrix} u_1(t) \\ u_2(t) \\ \dots \\ u_n(t) \end{bmatrix}. \quad (7)$$

In cases where one does not obtain a hall-sensor voltage for every strand, the strand currents cannot be directly obtained, and the calibration matrix will inevitably be reduced. However, one could still validate the model indirectly through the measurements conducted. Simulated currents using the LEM approach of eq. (4) can be used to estimate expected hall-sensor voltages using eq. (5). They can then be compared with what is being measured in reality. Moreover, it is essential to use the exact same circuit geometry for the calibration as for the measurement.

All cables were twisted and shielded, and each hall sensor had its own DC-current source to reduce measurement noise. The experiment had ten hall-sensors, i.e., one per strand for the conductors located in the left column (i.e., strands #1 to #10 in Fig. 3). Moreover, the right column (i.e., strands #11 to #20) will also perturb the measurements. Single-strand calibration measurements were conducted to obtain the calibration matrix's transfer function (i.e., a 10-by-20 matrix), according to eq. (6) to get rid of the perturbations. This process was repeated ten times per leg with a current spanning from 5 A to 60 A, covering the complete current measurement range.

Fig. 12 presents the key results of the experiments conducted. All the subfigures presents the hall sensor voltages (u_1 to u_{10}) versus total current. For u_1 to u_5 in Figs. 12 (a) and 12 (c), there is a good match for both the amplitude and the phase angle (except for u_2). However, the match is slightly worse for u_9 (especially the amplitude), presented in Figs. 12 (b) and 12 (d), but is good for the other voltages. It has been decided to widen only one column because even with the thermal camera confirmation, there is no absolute certainty that the current will be the same in the widened legs. In summary, except for two voltages (u_2 and u_9), the measurements fit well to very well with the simulations for both amplitude and phase.

Fig. 13 presents the amplitude and phase of the measured hall sensor voltage compared with different simulation models. Adding 3D stray elements significantly improved the simulation precision, which was an expected result as the measurement is a short-circuit measurement where any piece of resistance or inductance has an impact. It is possible to notice that the DSSIM performs really well against measurements, whereas the difference is smaller compared to the CSSIM in the 2D configuration. One can note that the more 3D elements are added to the simulation model, the better is the agreement between the measurements and the simulation. Tables IV and V presents the value of the considered 3D stray elements.

In the experiment, only one strand column has been

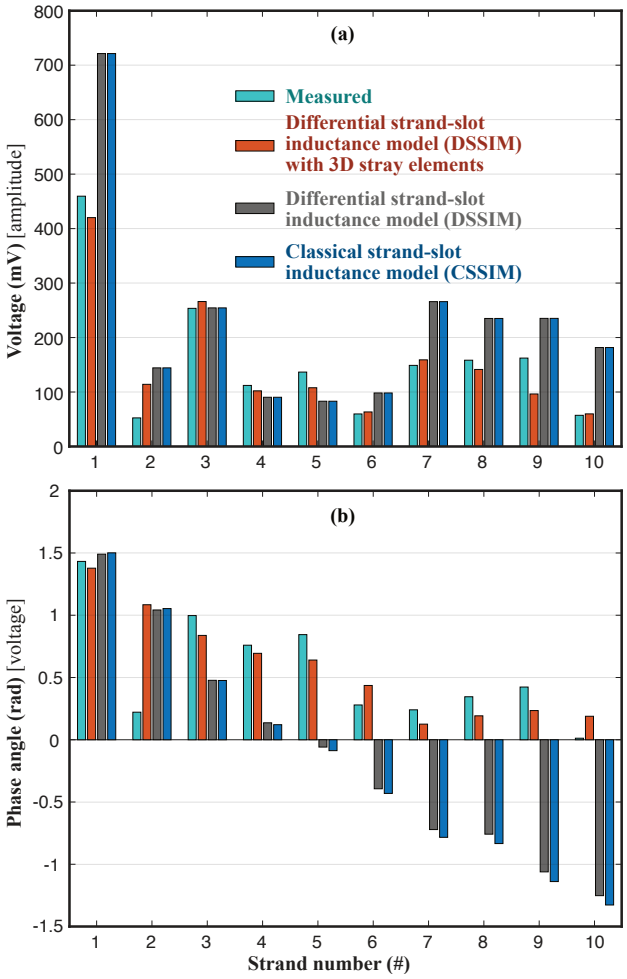

Fig. 13. Results for the 20-strand slot model where AC current loading penetrating the slot were 309.52 A (rms). **(a)**: Amplitude of hall-sensor voltage. **(b)**: Phase angle of hall-sensor voltage..

widened[3] incorporating all hall-sensors, which will have a slight impact on the measured voltages. The widening of the conductors has been tentatively taken into account in the parameters (i.e., resistances and inductance) simulation model (eq. 4), which could reduce the gap between simulation and measurements, but unfortunately, not close it completely. These aspects could be further explored in further investigations, as radically changing the design of such an experiment is not a very promising alternative. The first lesson is that there are limitations in the number of simultaneous recordings. Secondly, a reduction of the number of strands would lead to a significant reduction of the circulating current effect, which minimized the fruitfulness of the investigation.

The experiment slot could not be saturated, as large AC machines have only two bars per slot, and the current level in a laboratory is restricted. Making a multiturn slot would make the experiment unrealistic and add parasitic signals on the hall sensors, leading to the impossibility of carrying out any measurements. Keep in mind that in the actual setup,

[3]A measurement with only one hall sensor for two strands would lead to a kind of average value of both currents, which is not wanted. Moreover, the currents cannot be "controlled", which would lead to even worse results.

the measurement resolution is in the range of 10 mV/A [4]. So the experiment is conducted by basically comparing an ideal slot model with a highly permeable slot model. According to [16], there should be a small but measurable difference in circulating currents (basically in the same order of magnitude as Fig. 13).

VI. Conclusion

This paper presents and validates a proposed differential strand-slot inductance model (DSSIM) for large AC machines that take exact strand dimensions and iron core saturation (locally and globally) into account numerically. A simulation comparison between existing models shows its significant enhancement in numerical precision against alternatives (e.g., ASSIM and CSSIM). Moreover, the opportunities and limitations of the DSSIM have been demonstrated experimentally in a small-scale test segment that emulates a generic armature slot. The measurements show the improved accuracy of our proposed DSSIM with 3D stray elements. Small-scale experiments need complex modeling of their end part to exhibit errors when the measurement is non-invasive. It adds more uncertainties in our experimental proof, even though it has already been confirmed by time-stepping FEA. A precise and complete inductive-resistive model is needed to achieve a high fidelity agreement between the measurements and the simulations, especially including the 3D stray elements. Basically, the experiment is a short-circuit measurement where any resistive or inductive effect matters.

The most important findings are the following. The relative variation of the inductance, not the absolute value, makes the critical difference in circulating current computation, especially when inductive elements are dominant. The critical driver of circulating currents is the difference between the maximum and minimum value of the inductance. Roughly speaking, the mean value of the inductance gives an idea of the amplitude of the circulating currents, while the variation gives an idea of the relative split between the branches. Further research should increase the domain of use of LEMs for a complete circulating current prediction of AC machines by combining both the core and the end-winding, incorporating all relevant large-scale effects.

References

[1] M. W. Meiswinkel, A. Ebrahimi, C. Wohlers, and T. Neschitsch, "Transient roebel bar force calculation in large salient-pole synchronous machines," *IEEE Access*, vol. 9, pp. 2266–2273, Jan. 2021.

[2] M. Kowalski, S. Gertz, O. Mrkulic, and C. Kreischer, "Validation and application of magnetic sub-model techniques in turbogenerator end zones for local eddy current calculation in roebel bars," *IEEE Trans. Magn.*, vol. 56, no. 3, pp. 1–4, March 2020.

[3] C. Wang, Y. Liang, X. Bian, and Y. Wan, "Measuring method for strand current of stator bars based on search coils," *IEEE Trans. Ind. Electron.*, vol. 66, no. 9, pp. 7347–7355, Sept. 2019.

[4] Y. Liang, X. Bian, H. Yu, L. Wu, and L. Yang, "Analytic algorithm for strand slot leakage reactance of the transposition bar in an ac machine," *IEEE Trans. Ind. Electron.*, vol. 61, no. 10, pp. 5232–5240, Oct. 2014.

[5] Y. Liang, X. Bian, H. Yu, L. Wu, and B. Wang, "Analytical algorithm for strand end leakage reactance of transposition bar in ac machine," *IEEE Trans. Energy Convers.*, vol. 30, no. 2, pp. 533–540, June 2015.

[4] Using resistance instead would lead to a resolution of 0.5 mV/A, which is not in the measuring range available in the laboratory.

[6] F. Maurer and J. K. Nøland, "A rectangular end-winding model for enhanced circulating current prediction in ac machines," *IEEE Trans. Energy Convers.*, vol. 36, no. 1, pp. 291–299, March 2021.

[7] X. Bian, Y. Liang, and G. Li, "Analytical algorithm of calculating circulating currents between the strands of stator winding bars of large turbo-generators considering the air gap magnetic field entering stator slots," *IEEE Trans. Energy Convers.*, vol. 33, no. 1, pp. 32–39, March 2018.

[8] X. Bian and Y. Liang, "Circuit network model of stator transposition bar in large generators and calculation of circulating current," *IEEE Trans. Ind. Electron.*, vol. 62, no. 3, pp. 1392–1399, March 2015.

[9] Y. Liang and Y. Chen, "Circulating current losses analysis and improved incomplete transposition for stator bars in large hydro-generators," *IET Elect. Power Appl.*, vol. 10, no. 2, pp. 125–132, Feb. 2016.

[10] Y. Liang, L. Wu, X. Bian, and C. Wang, "Influence of void transposition structure on the leakage magnetic field and circulating current loss of stator bars in water-cooled turbo-generators," *IEEE Trans. Ind. Electron.*, vol. 63, no. 6, pp. 3389–3396, June 2016.

[11] Y. Liang, L. Wu, X. Bian, and H. Yu, "The influence of transposition angle on 3-d global domain magnetic field of stator bar in water-cooled turbo-generator," *IEEE Trans. Magn.*, vol. 51, no. 11, pp. 1–4, Nov. 2015.

[12] J. Haldemann, "Transpositions in stator bars of large turbogenerators," *IEEE Trans. Energy Convers.*, vol. 19, no. 3, pp. 553–560, Sept. 2004.

[13] J. Haldemann, "Stator winding of a directly cooled turbogenerator," Jul. 4 2017, US Patent App. 9,698,640.

[14] M. A. Iseli, "Stray losses in stator windings of large synchronous machines under consideration of transposition and end region field (Zusatzverluste in statorwicklungen grosser synchronmaschinen unter berücksichtigung der verdrillung und der stirnraumfelder)," Ph.D. dissertation, Dept. Inf. Tech. & Electr. Eng., ETH Zurich, Zurich, Switzerland, 1991.

[15] J. Haldemann, "Analysis of different transpositions in stator windings of large synchronous machines, their effects on the distribution of current and temperature and stray losses under different operating conditions (Untersuchung verschiedener verdrillungsarten in statorwicklungen großer synchronmaschinen, deren wirkung auf strom-und temperaturverteilung und zusatzverluste in verschiedenen betriebszuständen)," Ph.D. dissertation, Dept. Inf. Tech. & Electr. Eng., ETH Zurich, Zurich, Switzerland, 1997.

[16] F. M. Maurer, "Electrical effects in winding of large electrical ac machines application to advanced large size DFIM," Ph.D. dissertation, School of Eng., EPFL Lausanne, Lausanne, Switzerland, 2019.

[17] J.-W. Chin, K.-S. Cha, J.-C. Park, D.-M. Kim, J.-P. Hong, and M.-S. Lim, "Investigation of ac resistance on winding conductors in slot according to strands configuration," *IEEE Trans. Ind. Appl.*, vol. 57, no. 1, pp. 316–326, Jan.-Feb. 2021.

[18] L. Wang, B. Kou, and W. Cai, "Research on resistance enhancement coefficient and thermal dissipation of stator strands in huge synchronous generator," *IEEE Access*, vol. 8, pp. 40 357–40 366, March 2020.

[19] P. Yang, Y. Liang, X. Bian, and C. Zhou, "3-d thermal network model of stator transposed strands for a hydrogenerator," *IEEE Trans. Ind. Appl.*, vol. 57, no. 1, pp. 218–225, Jan. 2021.

[20] D. Wang, Y. Liang, L. Gao, X. Bian, and C. Wang, "A new global transposition method of stator winding and its loss calculation in ac machines," *IEEE Trans. Energy Convers.*, vol. 35, no. 1, pp. 149–156, March 2020.

[21] F. Maurer, B. Kawkabani, and J. K. Nøland, "Rapid 3-D magnetic integral field computation of current-carrying finite arc segments with rectangular cross section," *IEEE Trans. Magn.*, vol. 56, no. 2, 8100312, Feb. 2020.

[22] Y. Liang, X. Bian, L. Yang, and L. Wu, "Numerical calculation of circulating current losses in stator transposition bar of large hydrogenerator," *IET Sci. Meas. Technol.*, vol. 9, no. 4, pp. 485–491, July 2015.

[23] R. Wrobel, A. Mlot, and P. H. Mellor, "Contribution of end-winding proximity losses to temperature variation in electromagnetic devices," *IEEE Trans. Ind. Electron.*, vol. 59, no. 2, pp. 848–857, Feb. 2012.

[24] A. Lehikoinen and A. Arkkio, "Efficient finite-element computation of circulating currents in thin parallel strands," *IEEE Trans. Magn.*, vol. 52, no. 3, pp. 1–4, March 2016.

[25] A. Lehikoinen, N. Chiodetto, E. Lantto, A. Arkkio, and A. Belahcen, "Monte carlo analysis of circulating currents in random-wound electrical machines," *IEEE Trans. Magn.*, vol. 52, no. 8, pp. 1–12, Aug. 2016.

TABLE IV
NORMALIZED INDUCTANCE MATRIX FOR THE 3D STRAY ELEMENTS FIG. 13 WITH 0.221 μ H BASE OR 69.50 $\mu\Omega$ AT 50HZ SELF-REACTANCE. SELF-INDUCTANCES HIGHLIGHTED IN BOLD. THE CHOSEN BASE REPRESENTS THE VALUE OF THE HIGHEST INDUCTANCE.

	L01*	**L02***	**L03***	**L04***	**L05***	**L06***	**L07***	**L08***	**L09***	**L10***	**L11***	**L12***	**L13***	**L14***	**L15***	**L16***	**L17***	**L18***	**L19***	**L20***
L01*	**0.9991**	0.8521	0.7454	0.6710	0.6151	0.5623	0.5371	0.5155	0.4965	0.4796	0.6276	0.6226	0.6091	0.5945	0.5823	0.5572	0.5345	0.5145	0.4966	0.4804
L02*	0.8521	**0.9711**	0.8295	0.7274	0.6564	0.5924	0.5624	0.5373	0.5156	0.4966	0.6189	0.6307	0.6263	0.6139	0.6012	0.5764	0.5522	0.5307	0.5114	0.4940
L03*	0.7454	0.8295	**0.9440**	0.8079	0.7105	0.6294	0.5925	0.5625	0.5373	0.5156	0.6010	0.6220	0.6344	0.6310	0.6204	0.5968	0.5713	0.5483	0.5275	0.5088
L04*	0.6710	0.7274	0.8079	**0.9181**	0.7876	0.6768	0.6295	0.5926	0.5626	0.5373	0.5808	0.6040	0.6256	0.6389	0.6373	0.6175	0.5915	0.5672	0.5450	0.5248
L05*	0.6151	0.6564	0.7105	0.7876	**0.8933**	0.7415	0.6768	0.6295	0.5926	0.5626	0.5608	0.5837	0.6075	0.6300	0.6450	0.6359	0.6120	0.5874	0.5640	0.5423
L06*	0.5623	0.5924	0.6294	0.6768	**0.7415**	0.8936	0.7879	0.7109	0.6569	0.6156	0.5420	0.5637	0.5872	0.6119	0.6359	0.6450	0.6302	0.6077	0.5840	0.5612
L07*	0.5371	0.5624	0.5925	0.6295	0.6768	0.7879	**0.9184**	0.8084	0.7279	0.6716	0.5245	0.5448	0.5671	0.5914	0.6175	0.6374	0.6391	0.6258	0.6043	0.5812
L08*	0.5155	0.5373	0.5625	0.5926	0.6295	0.7109	0.8084	**0.9445**	0.8301	0.7460	0.5085	0.5273	0.5481	0.5712	0.5969	0.6205	0.6312	0.6347	0.6223	0.6014
L09*	0.4965	0.5156	0.5373	0.5626	0.5926	0.6569	0.7279	0.8301	**0.9718**	0.8528	0.4938	0.5112	0.5306	0.5522	0.5765	0.6014	0.6141	0.6267	0.6311	0.6194
L10*	0.4796	0.4966	0.5156	0.5373	0.5626	0.6156	0.6716	0.7460	0.8528	**1.0000**	0.4802	0.4965	0.5144	0.5345	0.5573	0.5825	0.5948	0.6094	0.6230	0.6281
L11*	0.6276	0.6189	0.6010	0.5808	0.5608	0.5420	0.5245	0.5085	0.4938	0.4802	**0.8700**	0.8040	0.7347	0.6843	0.6453	0.6137	0.5873	0.5645	0.5447	0.5271
L12*	0.6226	0.6307	0.6220	0.6040	0.5837	0.5637	0.5448	0.5273	0.5112	0.4965	0.8040	**0.8701**	0.8041	0.7347	0.6844	0.6454	0.6138	0.5873	0.5646	0.5447
L13*	0.6091	0.6263	0.6344	0.6256	0.6075	0.5872	0.5671	0.5481	0.5306	0.5144	0.7347	0.8041	**0.8701**	0.8041	0.7348	0.6844	0.6454	0.6138	0.5873	0.5646
L14*	0.5945	0.6139	0.6310	0.6389	0.6300	0.6119	0.5914	0.5712	0.5522	0.5345	0.6843	0.7347	0.8041	**0.8702**	0.8041	0.7348	0.6844	0.6454	0.6138	0.5873
L15*	0.5823	0.6012	0.6204	0.6373	0.6450	0.6359	0.6175	0.5969	0.5765	0.5573	0.6453	0.6844	0.7348	0.8041	**0.8702**	0.8042	0.7348	0.6845	0.6455	0.6138
L16*	0.5572	0.5764	0.5968	0.6175	0.6359	0.6450	0.6374	0.6205	0.6014	0.5825	0.6137	0.6454	0.6844	0.7348	0.8042	**0.8702**	0.8042	0.7349	0.6845	0.6455
L17*	0.5345	0.5522	0.5713	0.5915	0.6120	0.6302	0.6391	0.6312	0.6141	0.5948	0.5873	0.6138	0.6454	0.6844	0.7348	0.8042	**0.8703**	0.8042	0.7349	0.6845
L18*	0.5145	0.5307	0.5483	0.5672	0.5874	0.6077	0.6258	0.6347	0.6267	0.6094	0.5645	0.5873	0.6138	0.6454	0.6845	0.7349	0.8042	**0.8703**	0.8043	0.7349
L19*	0.4966	0.5114	0.5275	0.5450	0.5640	0.5840	0.6043	0.6223	0.6311	0.6230	0.5447	0.5646	0.5873	0.6138	0.6455	0.6845	0.7349	0.8043	**0.8703**	0.8043
L20*	0.4804	0.4940	0.5088	0.5248	0.5423	0.5612	0.5812	0.6014	0.6194	0.6281	0.5271	0.5447	0.5646	0.5873	0.6138	0.6455	0.6845	0.7349	0.8043	**0.8703**

TABLE V
NORMALIZED DC-RESISTIVE COMPONENTS FOR THE 3D STRAY ELEMENTS FIG. 13 WITH 188.962 $\mu\Omega$ BASE.

	R01	**R02**	**R03**	**R04**	**R05**	**R06**	**R07**	**R08**	**R09**	**R10**	**R11**	**R12**	**R13**	**R14**	**R15**	**R16**	**R17**	**R18**	**R19**	**R20**
2D model	1.000	1.000	1.000	1.000	1.000	1.000	1.000	1.000	1.000	1.000	1.000	1.000	1.000	1.000	1.000	1.000	1.000	1.000	1.000	1.000
3D stray	3.5408	3.3171	2.9705	2.8660	2.6354	2.6404	2.8809	2.9954	3.3518	3.5856	2.2477	2.2487	2.2506	2.2536	2.2576	2.2626	2.2685	2.2755	2.2834	2.2924

[26] C. Wang, Y. Liang, L. Ni, D. Wang, and X. Bian, "Calculation and analysis of the strands short-circuit in stator transposition bar for large generators," *IEEE Access*, vol. 7, pp. 36 132–36 139, Apr. 2019.

[27] S. E. Dallas, A. N. Safacas, and J. C. Kappatou, "Interturn stator faults analysis of a 200-mva hydrogenerator during transient operation using fem," *IEEE Trans. Energy Convers.*, vol. 26, no. 4, pp. 1151–1160, Dec. 2011.

[28] R. Romary, C. Demian, P. Schlupp, and J. Roger, "Offline and online methods for stator core fault detection in large generators," *IEEE Trans. Ind. Electron.*, vol. 60, no. 9, pp. 4084–4092, Sept. 2013.

[29] J.-Y. Ruan and S.-M. Wang, "Magnetizing curve estimation of induction motors in single-phase magnetization mode considering differential inductance effect," *IEEE Trans. Power Electron.*, vol. 31, no. 1, pp. 497–506, Jan. 2016.

[30] S. Keller, "Large low speed hydrogenerators-UMP and additional damper losses in eccentricity conditions," School of Eng., EPFL Lausanne, Lausanne, Switzerland, Tech. Rep., Apr. 13, 2007.

[31] G. A. Bànyai, "Advanced model for multiphase generators," School of Eng., EPFL Lausanne, Lausanne, Switzerland, Tech. Rep., Sept. 29, 2011.

Frederic Maurer received his M.Sc. degree in 2009 and the Ph.D. degree in 2019 from the Swiss Federal Institute of Technology in Lausanne (EPFL). Since April 2009, he is working for Alstom Hydro (now GE Hydro) in different positions: R&D engineer in the generator technology center, Lead electrical engineer, and technical project manager. Since February 2021, he is a guest researcher at the Department of Electric Power Engineering, Norwegian University of Science and Technology. His current research interests include circulating current, electromagnetics, improved utilization of electrical machines, transportation electrification, and electricity market design. Dr. Maurer serves as a Reviewer for the IEEE TRANSACTIONS ON ENERGY CONVERSION and the IEEE TRANSACTIONS ON INDUSTRIAL ELECTRONICS.

Jonas Kristiansen Nøland (S'14-M'17) was born in Drammen, Norway, in 1988. He received the M.Sc. degree in electric power engineering from the Chalmers University of Technology, Gothenburg, Sweden, in 2013, and the Ph.D. degree in engineering physics from Uppsala University, Uppsala, Sweden, in 2017. Since 2018, he has been an Associate Professor with the Department of Electric Power Engineering, Norwegian University of Science and Technology. His current research interests include excitation systems, improved utilization of electrical machines, high-power machinery for aircraft applications, Hyperloop propulsion and levitation, and transportation electrification in general. Dr. Nøland serves as an Editor for the IEEE TRANSACTIONS ON ENERGY CONVERSION and as an Associate Editor for the IEEE TRANSACTIONS ON INDUSTRIAL ELECTRONICS.